Draft manuscript (Nov. 96): to be revised

The Sensitivity of Atmospheric Correction of Reflectances to the Surface BRDF

Baoxin Hu, Wolfgang Wanner, and Alan H. Strahler

Center for Remote Sensing and Department of Geography, Boston University, Boston, MA

Abstract

This paper systematically studies the relationship between surface BRDF (Bidirectional Reflectance Distribution Function) retrieval and atmospheric correction. The study uses the atmospheric correction scheme of the Moderate Resolution Imaging Spectroradiometer (MODIS), and angular sampling expected for MODIS and MISR (Multiangle Imaging Spectro-Radiometer) for different land cover types and optical depths of aerosols. The results show the following two points. 1). Even for a non-turbid atmosphere, the assumption of a Lambertian surface in atmospheric correction causes large errors in the retrieved surface reflectances, such as from 1.7% to 7.6% in the red band. Thus, it is necessary to consider the surface anisotropic BRDF in atmospheric correction. 2). Surface BRDF retrieval and atmospheric correction can be coupled in a converging iteration loop, which improves the quality of atmospheric correction and of subsequent BRDF retrieval. For example, performing two steps of the iteration loop is already sufficient to obtain a mean error of only 0.89% in the retrieved surface reflectances for the atmosphere with the aerosol optical depth of 0.4 in the red band.

1. INTRODUCTION

In the solar spectrum, the signal received by a remote sensor doesn't reflect the true reflectance characteristics of surface objects, due to atmospheric effects. Thus, it is necessary to remove atmospheric effects in remote sensing applications.

Atmospheric effects on upward radiance for a cloudless sky can be computed as a solution to the atmospheric radiative transfer (RT) equation. The reflectance properties of surface objects provide a lower boundary condition for the RT equation. Most objects have anisotropic reflectances, which can be described by the bidirectional reflectance distribution function (BRDF). Generally, the RT equation is solved with a nonuniform and non-Lambertian boundary surface. The research of Case et al. (1953) indicated that decoupling the atmospheric RT from the transfer within surface objects is rigorously possible without the loss of accuracy, only if the boundary conditions for the atmospheric RT equation are appropriately specified. But the reflectance properties of the boundary surface can only be retrieved from the remotely sensed data after the removal of atmospheric effects. To resolve this interdependency between surface BRDF retrieval and atmospheric correction, most atmospheric correction methods assume that the surface is Lambertian. The atmospheric correction scheme of the MODIS (Moderate Resolution Imaging Spectroradiometer) couples atmospheric correction and surface BRDF retrieval by performing an iteration loop. In this scheme, atmospheric correction is first performed on MODIS observations under the assumption of an isotropic surface BRDF; the reflectances are then used to retrieve a new BRDF, and atmospheric correction is updated based on the new BRDF (Vermote et al., 1995).

In theory, this problem of specifying the correct boundary conditions at the atmosphere-surface interface is eliminated when a coupled system of atmosphere and the earth surface is considered for the RT analysis. A single radiative transfer model that includes radiative transfer in the atmosphere as well as at the Earth's surface is developed for a coupled system. But a coupled system is very complicated, and the discontinuity of the interface between the atmosphere and surface objects is handled in present coupled atmosphere-surface

RT equations as an area of multiple reflections between the atmosphere and any surface object (Myneni, et al., 1991; Liang et al., 1993). In addition, solving coupled RT equations requires many approximations and a large number of calculations (Asrar, 1989).

In this paper, we focus on atmospheric correction methods which decouple the atmospheric RT from the RT within surface objects. The important question for these atmospheric correction methods is whether it is necessary to take surface anisotropic reflectance properties into consideration in atmospheric correction, and if so, how to do it.

The research of Lee and Kaufman (1986) indicates that even for a nonturbid atmosphere, the assumption of a Lambertian surface leads to large errors in predicted upward radiance in the backscattering portion of the hemisphere, especially for large solar zenith angles. Their research is based on a savanna data set (Kriebel, 1977). Vermote et al. (1995) analyze the effect of surface anisotropic reflectances on atmospheric correction by using a Hapke model (Pinty et al, 1989). The model parameters are determined by fitting a field-measured directional reflectance data set of a plowed field (Kimes, 1985). Their results show that an adequate surface BRDF for use in atmospheric correction can be retrieved from the results of the atmospheric correction assuming a Lambertian surface. This iteration ultimately causes much smaller errors in the surface reflectances than the use of an atmospheric correction with the assumption of a Lambertian surface does. For example, the error is reduced from $10\% - 15\%$ to $2\% - 3\%$, when the aerosol optical depth is 0.23. We have conducted similar research using Ross-thick–Li-sparse model (Wanner et al., 1995) based on three simulated land cover types (tree-dominated, crop-dominated, and tree and crop half-mixed, respectively) and the angular sampling of MODIS/MISR over latitude 45^o north during a 9-day period around March 25 (Strahler et al., 1995). In our results, the assumption of an isotropic surface boundary in the atmospheric correction calculation leads to an error of about $2\% - 16\%$ in the retrieved surface reflectance in the red band for an atmosphere with aerosol optical depths at $550nm$ of 0.15, 0.3 and 0.5. A single iteration of a coupled surface BRDF retrieval and atmospheric correction iteration loop reduces the error to a range from 0.4% to 6.2%. All of this research indicate the necessity of taking surface BRDF into account in atmospheric correction. But this work is based on several specific cases with limited land cover types and angular samplings.

In this study, we systematically analyze the relationship between the surface BRDF retrieval and atmospheric correction by investigating the sensitivity of the retrieved surface reflectance to the input surface reflectance properties based on the atmospheric correction scheme of MODIS.

2. Theoretical Basis and Simulation data

In the atmospheric correction algorithm of MODIS (Vermote et al., 1995), the reflectance at the top of the atmosphere for the visible and near-infrared bands are expressed as

$$\begin{aligned}\rho_{toa}(\mu_s,\mu_v,\phi) &= \rho_0 + e^{-\tau/\mu_v}e^{-\tau/\mu_s}\rho_s(\mu_s,\mu_v,\phi) + e^{-\tau/\mu_v}t_d(\mu_s)\bar{\rho} + e^{-\tau/\mu_s}t_d(\mu_v)\bar{\rho'} \\ &\quad + t_d(\mu_s)t_d(\mu_v)\bar{\bar{\rho}} + \frac{(e^{-\tau/\mu_s}+t_d(\mu_s))(e^{-\tau/\mu_v}+t_d(\mu_v))S(\bar{\bar{\rho}})^2}{1-S\bar{\bar{\rho}}} \qquad (1)\end{aligned}$$

where ρ_{toa} is the reflectance at the top of the atmosphere; ρ_0 is the intrinsic atmospheric reflectance; ρ_s is the surface reflectance; S is the reflectance of the atmosphere for isotropic light entering the base of the atmosphere; μ_s is the cosine of the solar zenith angle, and μ_v is the cosine of the view zenith angle; ϕ is the azimuthal difference between the sun and view zenith angle; $e^{-\tau/\mu_s}$ and $t_d(\mu_s)$ are the downward direct and diffuse transmittance of the atmosphere along the path of the incoming solar beam, respectively; $e^{-\tau/\mu_v}$ and $t_d(\mu_v)$ are the upward direct and diffuse transmittance of the atmosphere in the viewing direction, respectively; τ is the atmospheric optical depth; $\bar{\rho}$, $\bar{\rho'}$, and $\bar{\bar{\rho}}$ are the surface hemispherical-directional, directional-hemispherical, and hemispherical-hemispherical reflectances, respectively, and couple

the atmospheric optical parameters and the surface reflectance properties. They are expressed in Equation (2-4).

$$\bar{\rho}(\mu_s,\mu_v,\phi)=\frac{\int_0^{2\pi}\int_0^1 \mu L\downarrow(\mu_s,\mu,\phi')\rho_s(\mu_s,\mu_v,\phi'-\phi)d\mu d\phi'}{\int_0^{2\pi}\int_0^1 \mu L\downarrow(\mu_s,\mu,\phi')d\mu d\phi'} \tag{2}$$

$$\bar{\rho}'(\mu_s,\mu_v,\phi)=\bar{\rho}(\mu_v,\mu_s,\phi) \tag{3}$$

$$\bar{\bar{\rho}}=\overline{\bar{\rho}'(\mu_s,\mu_v,\phi)}\approx\frac{\int_0^1\int_0^{2\pi}\int_0^1 \rho_s(\mu,\mu',\phi)\mu\mu' d\mu d\mu' d\phi}{\int_0^1\int_0^{2\pi}\int_0^1 \mu\mu' d\mu d\mu' d\phi} \tag{4}$$

where, $L\downarrow(\mu_s,\mu,\phi')$ is the downwelling diffuse irradiance with the sun at μ_s.

From these equations, we can note that, given atmospheric optical parameters and a series of surface reflectances estimated by other products or calculated by a BRDF model describing the bidirectional reflectances of the surface object, the coupled terms can be calculated and the atmospherically corrected surface reflectances can be obtained by solving Equation (1). Operationally, a BRDF model and the model parameters are first determined by the prior knowledge of surface objects or a prior product, and then these coupled terms are calculated. To give more weight to the actual observations than to the estimated surface BRDF used in the calculation of these coupled terms, equation (1) can be modified as follows:

$$\begin{aligned}\rho_{toa} &= \rho_0+e^{-\tau/\mu_v}e^{-\tau/\mu_s}\rho_s+\rho_s[e^{-\tau/\mu_v}t_d(\mu_s)\bar{\rho}^*+e^{-\tau/\mu_s}t_d(\mu_v)\bar{\rho}'^*+t_d(\mu_s)t_d(\mu_v)\bar{\bar{\rho}}^*\\ &\quad+\rho_s\frac{(e^{-\tau/\mu_s}+t_d(\mu_s))(e^{-\tau/\mu_v}+t_d(\mu_v))S(\bar{\bar{\rho}}^*)^2}{1-S\bar{\bar{\rho}}}]\end{aligned} \tag{5}$$

$$\begin{aligned}\bar{\rho}^* &= \frac{\bar{\rho}}{{\rho_s}^m}\\ \bar{\rho}'^* &= \frac{\bar{\rho}'}{{\rho_s}^m},\\ \bar{\bar{\rho}}^* &= \frac{\bar{\bar{\rho}}}{{\rho_s}^m}\end{aligned} \tag{6}$$

where, ${\rho_s}^m$ is a predicted surface reflectance, for example taken from a BRDF model. In this modified approach, only the shape of the surface BRDF influences the correction process and not the actual magnitude of the estimated surface BRDF. ρ_s can be obtained by solving equation (5).

When the surface is Lambertian, $\bar{\rho}^*=\bar{\rho}'^*=\bar{\bar{\rho}}^*=1$ and $\bar{\bar{\rho}}=\rho_s$. Thus, equation (5) can be simplified as

$$\rho_{toa}=\rho_0+\frac{(e^{-\tau/\mu_s}+t_d(\mu_s))(e^{-\tau/\mu_v}+t_d(\mu_v))\rho_s}{1-S\rho_s} \tag{7}$$

So, under the assumption of a Lambertian surface, ρ_s can easily be calculated using equation (7).

We accomplished this study using 6S (Vermote et al., 1994). In its forward mode, 6S can calculate the reflectance at the top of the atmosphere at a given viewing and illumination geometry according to equation (1). 6S also performs atmospheric correction in its inverse mode. Here we use its atmospheric correction based on the assumption of a Lambertian surface according to equation (7). This method is called a Lambertian-based atmospheric correction. We have added an atmospheric correction method which considers the surface BRDF based on equation (5) and uses a BRDF model, Ambrals (Algorithm for Modis Bidirectional Reflectance Anisotropics of the Land Surface) (Strahler et al., 1996). This method is called BRDF-based atmospheric correction.

In this study, we use the forward mode of 6S to calculate simulated observation data (ρ_{toa}) of MODIS and MISR using equation (1). To make our simulation convincing, the following various conditions are used

in this research.

1). Angular sampling. We use the angular samplings of MODIS and MISR for geographic locations from latitude 60^o south (-60^o) to latitude 60^o north ($+60^o$) at intervals of 15^o during a 16-day period around March 12. These angular samplings provide a good coverage of the view angle hemisphere, and a range of sun zenith angle from 20^o to 60^o.

2). Surface cover types. Four typical land cover types are analyzed here. They are a plowed field, a hard wheat field with 11 percent of coverage, a grass lawn (vegetation coverage: 97%; LAI: 9.9) and a hardwood forest (Kimes et al., 1983, 1985, and 1986). Bidirectional reflectances at a given angular sampling are calculated by fitting Ambrals to these field-measured data sets and determining the model parameters for these land cover types in the red and near-infrared bands. The solid lines in Figure 1 and Figure 2 show the BRDF plots in the principal plane in the red and near-infrared bands, respectively. As can be seen, these BRDF shapes are typical of most land cover types. For example, in the red band, there is a strong hotspot in the surface BRDF of bare soil and the field with a sparse vegetation coverage, and an evident bowl shape and hotspot for the dense crop field, grass lawn, and forest.

3). Atmospheric conditions. The simulated atmospheric conditions are for a continental aerosol model and the aerosol optical depths at $550nm$ of 0.1, 0.2 and 0.4. Based on some measurement data of aerosol optical depths (Kaufman et al., 1994), an optical depth of about 0.1 is typical for semidesert areas (without dust outbreaks) and for land areas in high latitudes ($> 30^o$), and optical depths of about $0.2-0.3$ are typical for tropic forest area during the dry season. Also research on maximum aerosol optical depths derived from NOAA AVHRR global coverage data indicates that aerosol optical depths are often over 0.3, with the highest value of about 2.0 occurring over south America and Africa (Vermote et al., 1996).

To clearly show the atmospheric effects, we calculate and display the root mean square error (rmse) between the true surface reflectances (ρ_s) and those at the top of the atmosphere (ρ_{toa}) at every given angular sample in the top plots in Figure 3 and Figure 4. Figure 5 and Figure 6 show the plots of the reflectances in the principal plane in the red and near-infrared band, respectively, to display how atmospheric scattering affects the shape of the surface BRDF. As anticipated, 1). the errors are larger in the red band than in the near infrared band, because atmospheric scattering decreases as wavelength increases, and the effect of the path radiance of the atmosphere is larger in relative to the smaller reflectances of vegetated land covers in the red band than to their larger reflectances in the near infrared band; 2). the errors increase with the increasing of the optical depth of aerosols (even for the atmosphere with the aerosol optical depth of 0.1, the errors are still very large, ranging from 3.0% in the hard wheat field to 124% in the hardwood forest in the red band), and the shape of the surface BRDF at the top of the atmosphere is far different from that of the true one, due to the effect of atmospheric scattering. These results show that atmospheric effects on remotely sensed data should be removed in remote sensing applications where absolute surface reflectances are needed.

3. The sensitivity of the retrieved surface reflectance to the input surface reflection properties

From equation (5), one can see that the surface BRDF influences the atmospheric correction through the terms $\bar{\rho}^*$, $\bar{\rho'}^*$ and $\bar{\bar{\rho}}^*$. To obtain the relationship between atmospheric correction and the surface BRDF retrieval, we investigate the sensitivity of the retrieved surface reflectance to these ratios. Assuming that an error occurs separately and simultaneously in $\bar{\rho}^*$, $\bar{\rho'}^*$, and $\bar{\bar{\rho}}^*$ on the order of 1%, we can calculate the rmse caused in the retrieved surface reflectances for a given angular sampling. For different angular sampling and land cover types, the sensitivity of the retrieved surface reflectance to these ratios is different. The mean values and ranges based on all the various cases studied are shown in Figure 7 and Figure 8 for the red and near-infrared bands, respectively.

In Figure 7 and Figure 8, the x-axis shows the relative errors(%) in input $\bar{\rho}^*$, $\bar{\rho'}^*$, $\bar{\bar{\rho}}^*$ and all them combined; the y-axis shows the mean rmse (%) between the true surface reflectances and the retrieved values, caused by these errors. The error bars show the range of the rmse in various cases investigated (different land cover types and latitudes). From these plots, one can see that the sensitivity of the retrieved surface reflectance is nearly linear to any error occurring in $\bar{\rho}^*$, $\bar{\rho'}^*$ and $\bar{\bar{\rho}}^*$. The approximate slope degree is shown in Table 1 and Table 2 for the red and near-infrared bands, respectively. One can also see that the retrieved surface reflectance is more sensitive to $\bar{\rho}^*$ and $\bar{\rho'}^*$ than to $\bar{\bar{\rho}}^*$. This is because the contributions of the surface hemispherical-directional reflectance (relating to $\bar{\rho}^*$) and directional-hemispherical reflectance (relating to $\bar{\rho'}^*$) to the upward radiance are larger than that of the surface hemispherical-hemispherical reflectance (relating to $\bar{\bar{\rho}}^*$). And the retrieved surface reflectance is much more sensitive to all them combined than to one of them. For example, for an aerosol optical depth of 0.2 in the red band, when a 8% error occurs in $\bar{\rho}^*$, $\bar{\rho'}^*$, and $\bar{\bar{\rho}}^*$, the error caused in the retrieved surface reflectance is 1.17%, 1.18%, and 0.44%, respectively. But, when the error simultaneously occurs in them, the error caused in the retrieved surface reflectance is 2.71%. Finally, one can see that the sensitivity of the retrieved surface reflectance to these ratios is larger in the red band than in the near-infrared band and increases as the optical depth of aerosols increases, and that the error bars indicate that the sensitivity of the retrieved surface reflectance to these ratios varies with the land cover types and angular samplings.

In the following, we will analyze the relationship between the surface BRDF retrieval and atmospheric correction by considering these results and atmospheric correction methods.

3.1. Lambertian-based atmospheric correction

A Lambertian-based atmospheric correction assumes the surface is Lambertian, where $\bar{\rho}^*$, $\bar{\rho'}^*$ and $\bar{\bar{\rho}}^*$ equal 1. We calculate the rmse in $\bar{\rho}^*$, $\bar{\rho'}^*$ and $\bar{\bar{\rho}}^*$ caused by this assumption for a given angular sampling. Column IV of Table 1 and Table II shows the mean rmses of all cases here (different land cover types and altitudes) for $\bar{\rho}^*$, $\bar{\rho'}^*$ and $\bar{\bar{\rho}}^*$ and their ranges (in brackets). Referring to the degrees in slope, we can see that the errors in $\bar{\rho}^*$, $\bar{\rho'}^*$ and $\bar{\bar{\rho}}^*$ will lead to large errors in the retrieved surface reflectance, such as from 1.8% to 7.7% for the aerosol optical depth of 0.1 in the red band. These points can be demonstrated by carrying out a Lambertian-based atmospheric correction.

We performed a Lambertian-based atmospheric correction for the ρ_{toa} calculated above using the inverse mode of 6S according to equation (7). Table 3 shows the mean and range values of the rmse(%) between the true surface reflectances and the retrieved values from this Lambertian-based atmospheric correction for a given angular sampling, and for the various cases. As the table shows, even in a non-turbid atmosphere, the error in the retrieved surface reflectance is still very large. For example, when the aerosol optical depth is 0.1, the mean value of the error is 1.90% and its maximum is as high as 4.10% in the near-infrared band, and the error increases to the mean value of 3.21% with the maximum of 7.66% in the red band. Furthermore, as the aerosol optical depth increases from 0.1 to 0.4, the mean error increases from 3.21% to 7.46% in the red band, and from 1.90% to 5.02% in the near-infrared band. Finally, the large error range indicates that the error varies with land cover types and angular samplings (i.e. the BRDF shapes). This point can clearly be seen from the middle plots in Figure 3 and Figure 4. For different land cover types at different angular samplings, the BRDF shape is different. Thus the error caused by the assumption of a Lambertian surface is different. The farther away from isotropy the surface BRDF shapes are, the larger the error is. Among these land cover types, the plowed field has the strongest anisotropic reflectance characteristics, thus the error caused in the plowed field is largest. The differences in the error caused in the surface reflectance in different cases become larger with the increasing of the optical depths of aerosols.

To see how the Lambertian-based atmospheric correction affects the BRDF shape, we show the BRDF plots in the principal plane in Figure 1 and Figure 2, where those with the dotted lines are retrieved from the Lambertian-based atmospheric correction. From these plots, we can note that the Lambertian-based

atmospheric correction distorts the BRDF shapes and the largest errors occur at the hotspot and bowl edge area. But the BRDF shapes retrieved from the Lambertian-based atmospheric correction are indeed nearer to the true ones than an isotropic line.

Surface reflectances retrieved from atmospheric correction are usually used to invert a BRDF model and then retrieve some biophysical parameters of surface objects and calculate the surface albedo. So, we also calculate the rmses between the true model parameters and their retrieved values, and between the true surface albedo and its predicted value by the inverted BRDF model. The results are shown in Table 3.

From Table 3, we can see that the errors in the retrieved model parameters are very large, such as 13.58% for the aerosol optical depth of 0.1 in the red band. The albedo predicted by the retrieved BRDF model deviates from its true value by 0.03% to 4.88% in the red band for various cases (different latitudes, land cover types and aerosol optical depths), and by 0.21% to 4.61% in the near-infrared band.

From the above analysis of surface reflectances at given angular samples, BRDF model parameters and surface albedos, we can see that one should take the surface BRDF into account in atmospheric correction.

3.2. The coupled surface BRDF retrieval and atmospheric correction loop

The coupled surface BRDF retrieval and atmospheric correction iteration loop uses a surface BRDF in atmospheric correction as a lower boundary condition in the atmospheric correction. As in all iteration procedures, initial values of input surface reflectance properties are first determined, and then the iteration is performed and the estimated values are updated. The iteration is continually performed until a desirable result is obtained. Here, the initial values of $\bar{\rho}^*$, $\bar{\rho'}^*$ and $\bar{\bar{\rho}}^*$ are estimated from the results of a Lambertian-based atmospheric correction. So, the first iteration of the loop consists of using Ambrals to fit the reflectances retrieved from the Lambertian-based atmospheric correction to obtain model parameters. Based on these model parameters and the atmospheric optical parameters, the estimated $\bar{\rho}^*$, $\bar{\rho'}^*$ and $\bar{\bar{\rho}}^*$ can be calculated. Then BRDF-based atmospheric correction of ρ_{toa} is performed. From the previous calculations, we know, this Lambertian-based atmospheric correction leads to large errors in the model parameters (Table 3). However, the errors caused in $\bar{\rho}^*$, $\bar{\rho'}^*$ and $\bar{\bar{\rho}}^*$ by using these model parameters is acceptable.

Column V of Table 1 and Table 2 show the errors between the true $\bar{\rho}^*$, $\bar{\rho'}^*$ and $\bar{\bar{\rho}}^*$ and the estimated values from a Lambertian-based atmospheric correction. Compared with Column IV (the errors in $\bar{\rho}^*$, $\bar{\rho'}^*$ and $\bar{\bar{\rho}}^*$ caused by the assumption of a Lambertian surface in the Lambertian based atmospheric correction), the errors in Column V are smaller, thus causing smaller errors in the retrieved surface reflectance (referring to the slope degrees). But when the optical depth of aerosols is large, such as 0.4, the errors in the retrieved surface reflectance are still large, such as a mean value of about 2.50% in the red band (referring to the slope degrees).

The errors caused in the retrieved surface reflectances, BRDF model parameters and surface albedos after performing the first iteration are shown in Table 4. Compared with the errors caused by the Lambertian-based atmospheric correction in Table 3, the errors shown in Table 4 caused by the first iteration are much smaller. For example, in the red band, the mean error in the retrieved surface reflectance decreases from 3.21% – 7.46% to 0.49% – 2.64%. Also the ranges of these errors are smaller, which can be seen in the bottom plots in Figure 3 and Figure 4. This is because the surface reflectance properties used in the first iteration are nearer to the true ones than those used in Lambertian-based atmospheric correction, thus the difference in the extent to which the estimated BRDF shapes deviates from the the actual ones for different cases is decreased. After the first iteration, the surface BRDF shape in the principal plane is much nearer to the true one than it is after a Lambertian-based atmospheric correction. This is demonstrated in Figure 1 and Figure 2, where the dashed lines are the results after the first iteration.

From Table 4, one can also note that the errors are still large in the retrieved surface reflectances, such as over 2.00% in the red band in some cases when the aerosol optical depth is larger than 0.2. Therefore, we explored the effects of a second iteration in this procedure.

In this step, the Ambrals BRDF models are fitted to the surface reflectances retrieved from the first iteration. Because the errors in the model parameters inverted from the first iteration are much smaller than those from the Lambertian-based atmospheric correction, in this step the errors in $\bar{\rho}^*$, $\bar{\rho'}^*$ and $\bar{\bar{\rho}}^*$ calculated based on these model parameters should be smaller than those in the first iteration. Thus the errors caused in the retrieved surface reflectances are smaller than those occurring after the first iteration. This is demonstrated by the values in column VI of Table 1 and Table 2 , and Table 5. The mean errors in $\bar{\rho}^*$, $\bar{\rho'}^*$ and $\bar{\bar{\rho}}^*$ decrease from 4.08%, 4.02% and 6.99% in the first iteration to 1.45%, 1.46% and 2.39% in the second iteration, for an atmosphere with the aerosol optical depth of 0.4 in the red band. Correspondingly, the mean errors in the retrieved surface reflectances decrease from 2.64% to 0.90%. The errors caused in the model parameters and surface albedos also decrease. However, the error ranges in the retrieved surface reflectances tell us that for certain extreme cases (such as MODIS/MISR looks over 60° north and south), the error of the retrieved surface reflectances of the plowed field is over 3.60% in the red band. Actually, depending on specific land cover types and the angular sampling, the iteration loop may need to be performed more than two times. Thus the convergency of the iteration loop should be considered.

Because of the complication of the algorithm, we can not obtain proofs mathematically. Thus, in this study, we iteratively perform the iteration loop several times for an aerosol optical depth of 0.4. For every step, we use Ambrals to fit the reflectances retrieved from the last step and do a BRDF-based atmospheric correction based on the inversion results. The rmse between the true surface reflectances and the retrieved values, and the relative change in the model parameters between the adjacent steps, decreases as more iterations are performed. After 5 iterations, the relative change in the model parameters decreases to 0.5% and the mean error in the retrieved surface reflectances decrease to near-infrared band than in the red band.

In summary, surface BRDF retrieval and atmospheric correction can be coupled in a converging iteration loop, which can improve the quality of atmospheric correction of reflectances.

4. DISCUSSION

4.1. The effect of skylight on atmospheric correction

From equation (2), we know the calculation of $\bar{\rho}$ requires knowledge of the downward radiation. Thus in a BRDF-based atmospheric correction, the exact distribution of skylight need to be known. Here we will investigate the assumption that the skylight is isotropic, so that we can save a large amount of calculation time. We use the model parameters retrieved from Lambertian-based atmospheric correction and assume the skylight is isotropic to calculate the estimated $\bar{\rho}^*$. Table 6 is the mean rmse and dynamic range between the estimated $\bar{\rho}^*$ and the true values. Compared with column V in Table 1 and Table 2 where the skylight is exactly calculated, the estimated error in $\bar{\rho}^*$ increases from $0.77\% - 5.66\%$ to $5.16\% - 16.02\%$ to the aerosol optical depth of 0.1 in the red band. Thus the corresponding error caused in the surface reflectances by the error in $\bar{\rho}^*$ increases from $0.08\% - 0.57\%$ to $0.52\% - 1.60\%$. Thus we should avoid the assumption of an isotropic skylight in atmospheric correction.

4.2. Comparison between the BRDF-based atmospheric correction using absolute surface BRDF and that using surface BRDF shape

Table 1 and Table 3 show the rmse between the true ratio of the surface albedo to its bidirectional reflectance, $\bar{\bar{\rho}}^*$, and the estimated ratio from the results of the Lambertian-based atmospheric correction, and that between the true surface albedo, $\bar{\bar{\rho}}$, and its estimated values from the results of the Lambertian-based atmospheric correction, respectively. From these results, we can note that the rmse in $\bar{\bar{\rho}}$ is smaller than that in $\bar{\bar{\rho}}^*$. Similarly, we also calculate the estimated errors in $\bar{\rho}$ and $\bar{\rho'}$ in the first iteration of the loop. The results are shown in Table 7. Compared with column V of Table 1, the errors in $\bar{\rho}$ and $\bar{\rho'}$ are

smaller than those in $\bar{\rho}^*$ and $\bar{\rho}'^*$. So a question remains, is the BRDF-based atmospheric correction based on Equation (7) better than that based on Equation (1)? To answer this question, we analyze the sensitivity of the retrieved surface reflectance to $\bar{\rho}$, $\bar{\rho}'$ and $\bar{\bar{\rho}}$ according to Equation (1) under the same simulation conditions as those in the above sensitivity analysis. Figure 7 shows the results in the red band. Comparing Figure 7 and Figure 5, one can see that the surface reflectance is more sensitive to $\bar{\rho}$, $\bar{\rho}'$ and $\bar{\bar{\rho}}$ than to $\bar{\rho}^*$, $\bar{\rho}'^*$ and $\bar{\bar{\rho}}^*$. Thus even though the estimated errors in $\bar{\rho}$, $\bar{\rho}'$ and $\bar{\bar{\rho}}$ are smaller than those in $\bar{\rho}^*$, $\bar{\rho}'^*$ and $\bar{\bar{\rho}}^*$, the error caused in the surface reflectances is larger by the errors in $\bar{\rho}$, $\bar{\rho}'$ and $\bar{\bar{\rho}}$ than by the errors in $\bar{\rho}^*$, $\bar{\rho}'^*$ and $\bar{\bar{\rho}}^*$. The BRDF-based atmospheric correction using the estimated surface BRDF shapes is better than that using absolute surface BRDF.

5. Conclusions

In this study, we analyze the sensitivity of atmospherically corrected reflectances to surface BRDF. Decoupling atmospheric correction and the surface anisotropic BRDF leads to large errors in the retrieved surface reflectances. In addition to atmospheric optical parameters, surface BRDF shape determines the size of the error, varying from 2.41% to 11.64% in the red band for the atmosphere with the aerosol optical depth of 0.2. The farther away from isotropy the BRDF shape is, the larger the error becomes. The surface BRDF retrieval and atmospheric correction can be coupled in a converging iteration loop. The initial values of surface reflectance properties are derived from the atmospheric correction with the assumption of a Lambertian surface. The accuracy of the estimated surface reflectance properties increases as more iterations are performed, thus the error in the retrieved surface reflectance decreases. However, one or two iterations are already sufficient to obtain a mean error of only 0.89% in the red band even with an atmospheric optical depth of 0.4.

As one notes, all the error values in this study are based on the assumption that the exact atmospheric optical parameters are known. This does not hold in actual applications. In the future, we will further analyze the effect of the uncertainty of atmospheric optical parameters on the sensitivity of atmospheric correction of reflectances to the surface BRDF.

We wish to thank Xiaowen Li, Crystal Schaaf, and other members of the MODIS BRDF/albedo team for their support and numerous discussions. This work was supported by NASA under NAS5-31369.

REFERENCES

Asrar, Ghassem, Theory and Applications of Optical Remote Sensing, A Wiley-Interscience Publication, 1989.

Case, R.M., F. de Hoffmane and G. Placzek, Introduction to the theory of neutron diffusion, vol.1, Los Alamos Scientific Laboratory, 1953.

Lee, T. Y. and Y. J. Kaufman, Non-Lambertian effects in remote sensing of surface reflectance and vegetation index, IEEE trans. Geosci. Remote Sens., 24, 699-708, 1986.

Liang S. and A. H. Strahler, Calculation of the angular radiation distribution for a coupled atmosphere and canopy, IEEE trans. Geosci. Remote Sens., 31, 491-502, 1993.

Kaufman Y. J., A. Gitelson, A. Karnieli, E. Ganor, R. S. Fraser, T. Nakajima, S. Mattoo, and B. N. Holben, Size distribution and scattering phase function of aerosol particles retrieved from sky brightness measurements, J. Geophys. Res., 100, 10341-10356, 1994.

Kimes, D. S., A. G. Kerber and P. J. Seller, Dynamics of directional reflectance factor distribution for vegetation canopies, Appl. Opt., 22(9), 1364-1372, 1983.

Kimes, D. S., W. W. Newcomb, C. J. Tucker, I. S. Zonneveldt, W. van Wijngaarden, J. de Leeuw, and G. F. Epema, Directional reflectance factor distributions for cover types of Northern Africa, Remote Sens. Environ 18, 1-19,1985.

Kimes, D. S., W. W. Newcomb, R. F. Nelson, and J. B. Schutt, Directional reflectance distributions of a hardwood and a pine forest canopy, IEEE Trans. Geosci. Remote Sens. GE-24, 281-293, 1986.

Kriebel, K. T., Measured spectral bidirectional reflection properties of four vegetated surfaces, Appl. Optics, 17(2), 352-259, 1978.

Myneni, R. B. and J. Ross, Photon-Vegetation Interactions", Springer- Verlag, 1991.

Pinty, B., Verstraete, M. M. and Dickinso, R. E., A physical model for predicting bidirectional reflectances over bare soil, Remote Sens. Env., 27, 273-288, 1989.

Strahler, A. H., Barnsley M. J., d'Entremont R., Hu B., Lewis P., Li X., Muller J., Schaaf, C. B., Wanner W. and Zhang B., MODIS BRDF/ Albedo Product: Algorithm Theoretical Basis Document Version 3.2, NASA EOS-MODIS, 1995.

Vermote, E. F., D. Tanre, Deuze, J. L. Herman, M. and Morcrette, J. J., Second Simulation of the Satellite Signal in the Solar Spectrum (6S), 6S User Guide Version 0, NASA-Goddard Space Flight Center-Code 923, Greenbelt, MD 20771, 1994.

Vermote, E. F., L. A. Remer, C. O. Justice, Y. J. Kaufman, and D. Tanre, Algorithm technical background Document: atmospheric correction algorithm, Modis Science Team and Associates, 1995.

Vermote, E. F., N. El Saleous, C. O. Justice, Y. J. Kaufman, J. L. Privette, L. Remer, J. C. Roger, and D. Tanre, Atmospheric correction of visible to middle infrared EOS-MODIS data over land surface: background, operational algorithm and validation, J. Geophys. Res., in press, 1996.

Wanner, W., X. Li, A. H. Strahler, On the derivation of kernels for kernel-driven models of bidirectional reflectance, J. Geophys. Res., 100, 21077-21089, 1995.

Table 1 The rmse(%) in $\bar{\rho}^*$, $\bar{\rho'}^*$ and $\bar{\bar{\rho}}^*$ in the red band

		slope degree	Lambertian assumption	BRDF(I)	BRDF (II)
$\bar{\rho}^*$	$\tau = 0.1$	0.10	13.42(7.06 – 27.68)	2.09(0.77 – 5.66)	0.28(0.09 – 0.94)
	$\tau = 0.2$	0.15	12.35(6.31 – 26.86)	2.78(1.00 – 7.84)	0.62(0.17 – 1.95)
	$\tau = 0.4$	0.20	11.99(6.19 – 27.92)	4.08(1.51 – 11.82)	1.45(0.43 – 4.75)
$\bar{\rho'}^*$	$\tau = 0.1$	0.10	13.35(6.99 – 28.50)	1.85(0.62 – 5.97)	0.29(0.09 – 1.07)
	$\tau = 0.2$	0.15	12.10(6.00 – 26.83)	2.56(0.89 – 8.32)	0.60(0.18 – 2.28)
	$\tau = 0.4$	0.20	11.58(5.59 – 26.88)	4.02(1.51 – 12.13)	1.46(0.45 – 5.33)
$\bar{\bar{\rho}}^*$	$\tau = 0.1$	0.03	23.91(14.34 – 56.53)	2.95(1.11 – 8.24)	0.43(0.16 – 1.36)
	$\tau = 0.2$	0.05	23.91(14.34 – 56.53)	4.15(1.65 – 12.17)	0.92(0.35 – 3.03)
	$\tau = 0.4$	0.12	23.91(14.34 – 56.53)	6.99(2.84 – 19.02)	2.39(0.88 – 7.47)

BRDF (I) and BRDF (II) represent the first and second iteration of the surface BRDF retrieval and atmospheric correction loop, respectively.

Table 2 The rmse(%) in $\bar{\rho}^*$, $\bar{\rho'}^*$ and $\bar{\bar{\rho}}^*$ in the near-infrared band

		slope degree	Lambertian assumption	BRDF(I)	BRDF (II)
$\bar{\rho}^*$	$\tau = 0.1$	0.06	12.56(6.99 – 23.79)	1.11(0.51 – 2.92)	0.12(0.04 – 0.47)
	$\tau = 0.2$	0.10	11.92(6.57 – 23.71)	1.74(0.82 – 4.62)	0.28(0.11 – 1.32)
	$\tau = 0.4$	0.16	11.64(5.85 – 24.98)	2.69(1.24 – 7.72)	0.67(0.32 – 2.04)
$\bar{\rho'}^*$	$\tau = 0.1$	0.06	11.19(4.40 – 25.06)	0.91(0.32 – 3.31)	0.10(0.04 – 0.34)
	$\tau = 0.2$	0.10	10.34(4.25 – 24.23)	1.45(0.39 – 5.24)	0.25(0.09 – 0.90)
	$\tau = 0.4$	0.16	9.89(4.33 – 24.54)	2.56(0.85 – 8.42)	0.67(0.29 – 2.53)
$\bar{\bar{\rho}}^*$	$\tau = 0.1$	0.03	20.49(11.24 – 55.51)	1.64(0.64 – 4.63)	0.17(0.07 – 0.58)
	$\tau = 0.2$	0.05	20.49(11.24 – 55.51)	2.70(1.05 – 7.62)	0.45(0.19 – 1.70)
	$\tau = 0.4$	0.10	20.49(11.24 – 55.51)	4.45(1.26 – 12.90)	1.14(0.53 – 3.45)

BRDF (I) and BRDF (II) represent the first and second iteration of the surface BRDF retrieval and atmospheric correction loop, respectively.

Table 3 The rmse(%) between the true BRDF, BRDF model parameters and surface albedo and their retrieved values from the Lambertian-based atmospheric correction

item	wavelength	$\tau = 0.1$	$\tau = 0.2$	$\tau = 0.4$
BRDF	red	3.21 (1.71-7.66)	4.73 (2.41-11.64)	7.46 (3.78-18.25)
	nir	1.90 (0.93-4.10)	3.05 (1.51-6.96)	5.02 (2.55-12.32)
model parameters	red	13.58 (10.40-22.48)	17.83 (10.87-30.01)	30.17 (24.85-41.67)
	nir	8.65 (5.82-10.83)	13.28 (9.51-19.96)	22.85 (16.74-31.44)
albedo	red	1.12 (0.03-2.95)	1.49 (0.10-3.43)	1.75 (0.20-4.88)
	nir	1.45 (0.21-2.55)	1.88 (0.41-3.01)	2.33 (0.10-4.62)

Table 4 The rmse(%) between the true BRDF, BRDF model parameters and surface albedo and their retrieved values from the first iteration of the coupled surface BRDF retrieval and atmospheric correction loop

item	wavelength	$\tau = 0.1$	$\tau = 0.2$	$\tau = 0.4$
BRDF	red	0.49 (0.16-1.85)	1.05 (0.32-3.92)	2.64 (0.84-9.08)
	nir	0.17 (0.09-0.60)	0.45 (0.26-1.34)	1.25 (0.56-1.64)
model parameters	red	1.66 (1.12-2.65)	3.69 (2.56-5.69)	9.72 (6.99-14.49)
	nir	0.74 (0.34-1.16)	1.87 (0.94-2.78)	5.17 (3.00-7.99)
albedo	red	0.36 (0.01-0.86)	0.68 (0.01-1.66)	1.33 (0.10-3.21)
	nir	0.15 (0.00-0.33)	0.32 (0.02-0.70)	0.70 (0.02-1.74)

Table 5 The rmse(%) between the true BRDF, BRDF model parameters and surface albedo and their retrieved values from the second iterations of the coupled surface BRDF retrieval and atmospheric correction loop

item	wavelength	$\tau = 0.1$	$\tau = 0.2$	$\tau = 0.4$
BRDF	red	0.07 (0.02-0.31)	0.23 (0.07-0.99)	0.90 (0.25-3.63)
	nir	0.02 (0.01-0.06)	0.07 (0.02-0.25)	0.34 (0.13-1.19)
model parameters	red	0.21 (0.11-0.46)	0.77 (0.43-1.14)	3.30 (1.96-8.11)
	nir	0.06 (0.02-0.14)	0.26 (0.10-0.40)	1.25 (0.56-2.22)
albedo	red	0.06 (0.01-0.15)	0.15 (0.01-0.43)	0.48 (0.01-1.35)
	nir	0.02 (0.00-0.03)	0.05 (0.00-0.11)	0.23 (0.01-0.88)

Table 6 The rmse(%) in $\bar{\rho}^*$ in the first iteration under the assumption of an isotropic skylight

wavelength	$\tau = 0.1$	$\tau = 0.2$	$\tau = 0.4$
red	9.22 (5.16-16.02)	8.54 (4.29-15.76)	7.20 (3.48-12.33)
nir	10.03 (3.49-17.60)	9.33 (2.61-16.28)	8.22 (2.03-5.64)

Table 7 The rmse(%) in $\bar{\rho}$ and $\bar{\rho}'$ in the red band in the first iteration of the coupled surface BRDF retrieval and atmospheric correction loop

	$\tau = 0.1$	$\tau = 0.2$	$\tau = 0.4$
$\bar{\rho}$	1.78 (0.80-4.56)	2.63 (1.28-5.17)	3.87 (2.15-8.10)
$\bar{\rho}'$	1.71 (0.81-4.36)	2.47 (1.34-5.00)	3.77 (2.21-7.94)

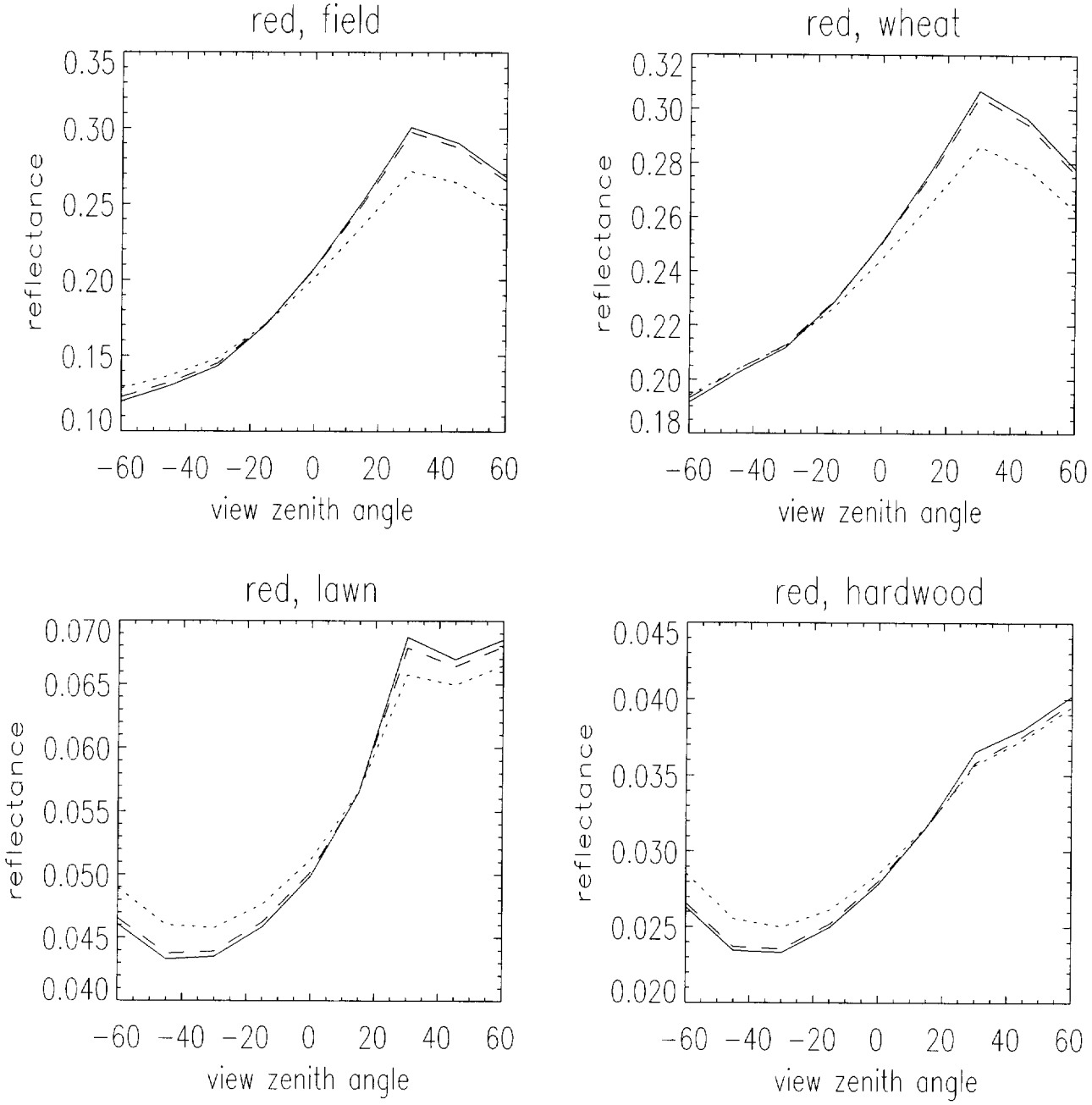

Fig. 1 The BRDF in the Principal Plane for selected Kimes data in the red band, where the sun zenith angle is 30° and aerosol optical depth is 0.2. solid line: true value; dotted line: the retrieved values through Lambertian-based atmospheric correction; dashed: the retrieved values through the first step of the surface BRDF retrieval and atmospheric correction loop

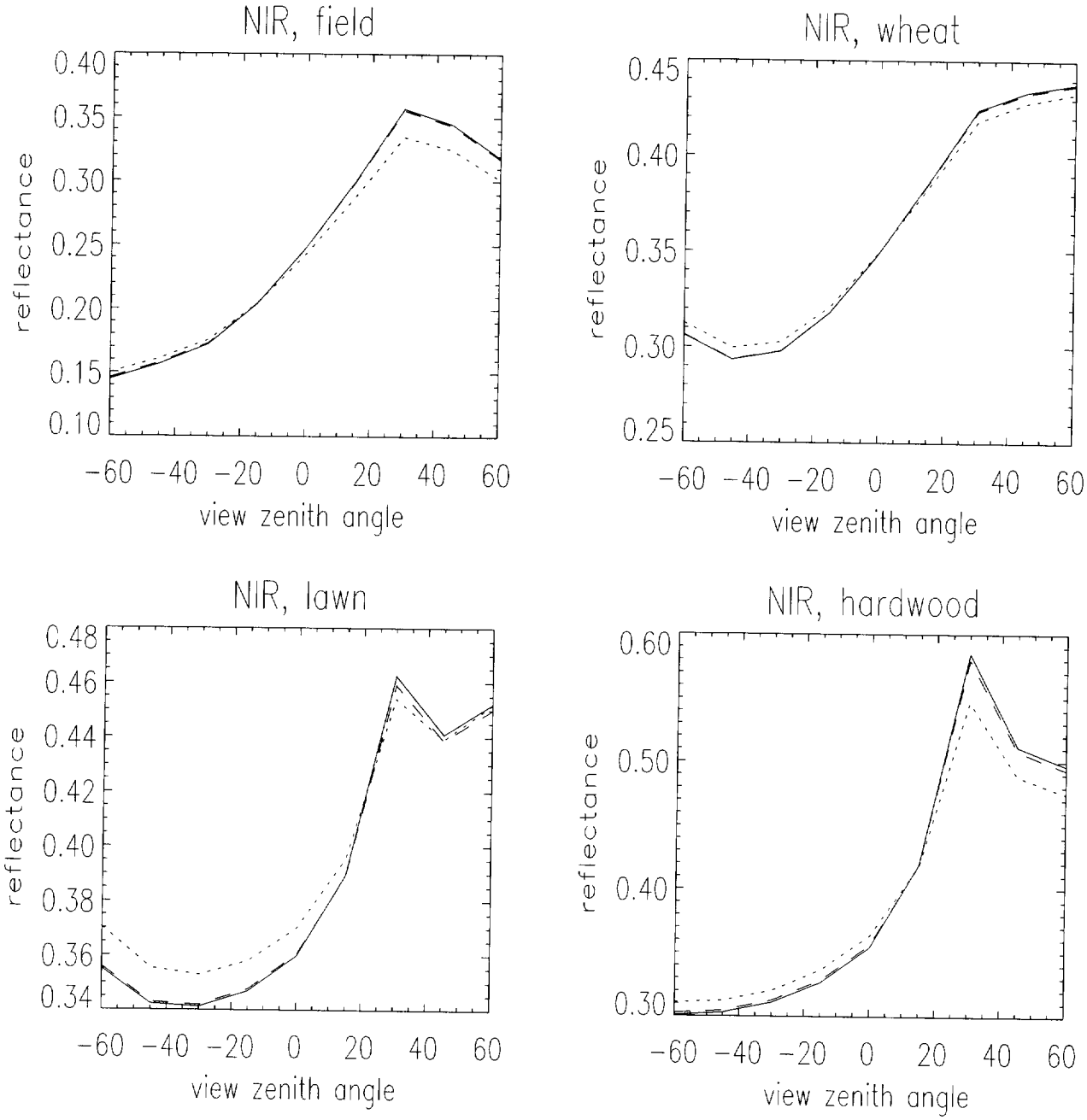

Fig. 2 The BRDF in the Principal Plane for selected Kimes data in the near-infrared band, where the sun zenith angle is 30° and aerosol optical depth is 0.2. solid line: true value; dotted line: the retrieved values through Lambertian-based atmospheric correction; dashed: the retrieved values through the first step of the surface BRDF retrieval and atmospheric correction loop

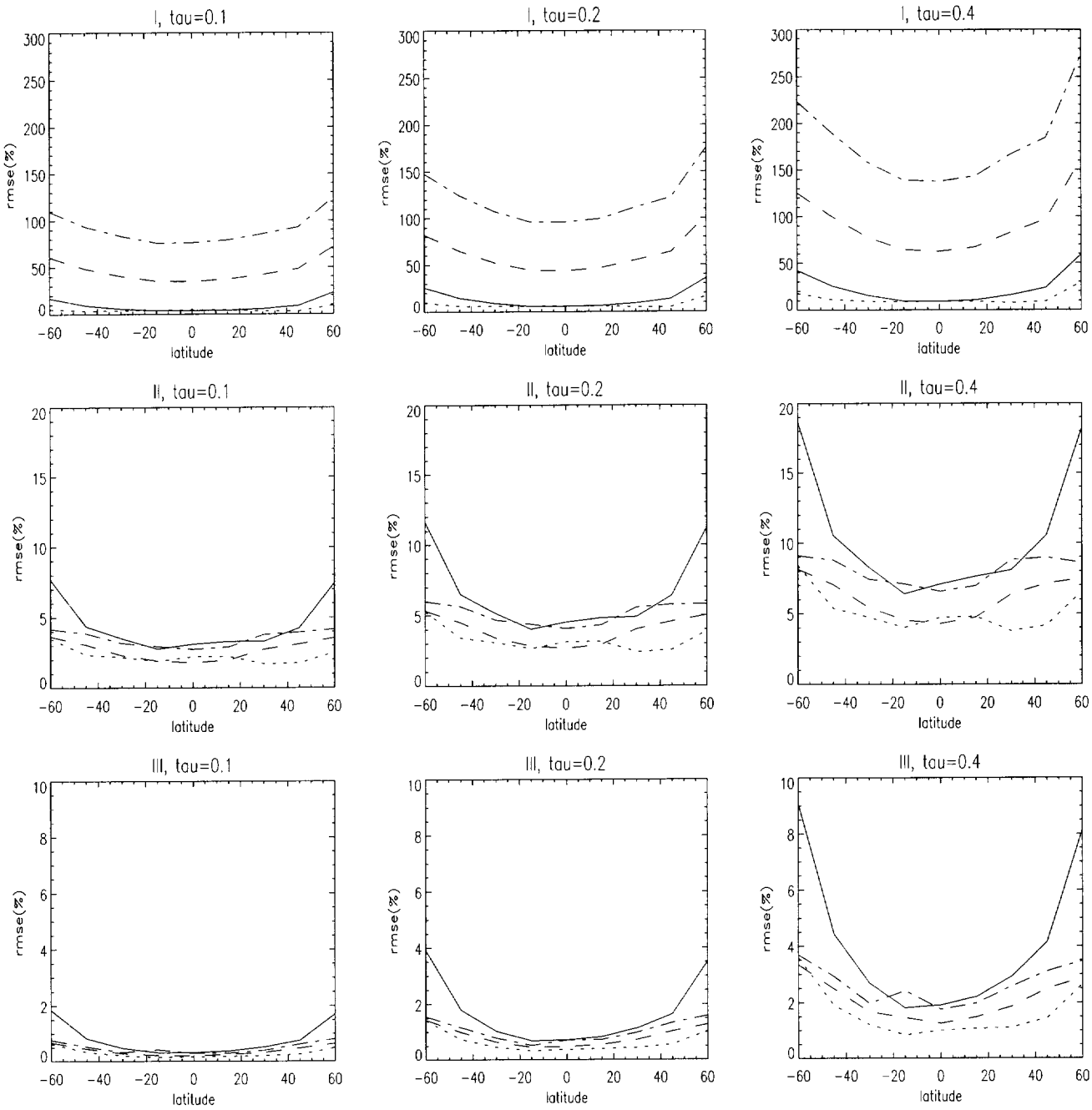

Fig. 3 The rmse between the retrieved surface reflectances and their true values in the red band. solid line: plowed field; dotted line: hard wheat; dashed line: grass lawn; dash-dotted line: hardwood. I, II and III denote the rmse between the true surface reflectances and the reflectances at the top of the atmosphere, the retrieved reflectances from Lambertian-based atmospheric correction, and the retrieved reflectances from the first step of the surface BRDF retrieval and atmospheric correction iteration loop, respectively.

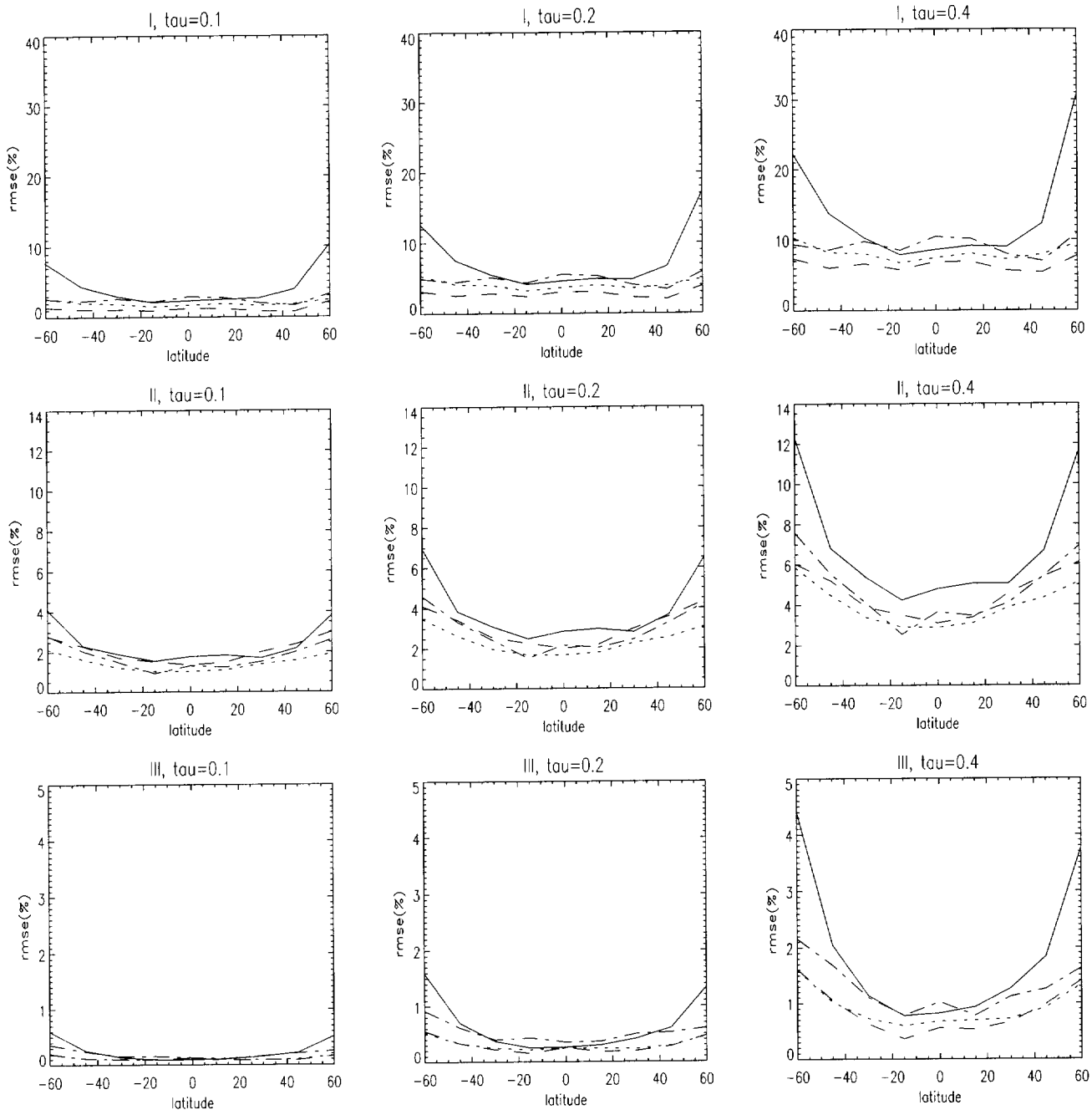

Fig. 4 The rmse between the retrieved surface reflectances and their true values in the near-infrared band. solid line: plowed field; dotted line: hard wheat; dashed line: grass lawn; dash-dotted line: hardwood. I, II and III denote the rmse between the true surface reflectances and the reflectances at the top of the atmosphere, the retrieved reflectances from Lambertian-based atmospheric correction, and the first step of the the surface BRDF retrieval and atmospheric correction iteration loop, respectively.

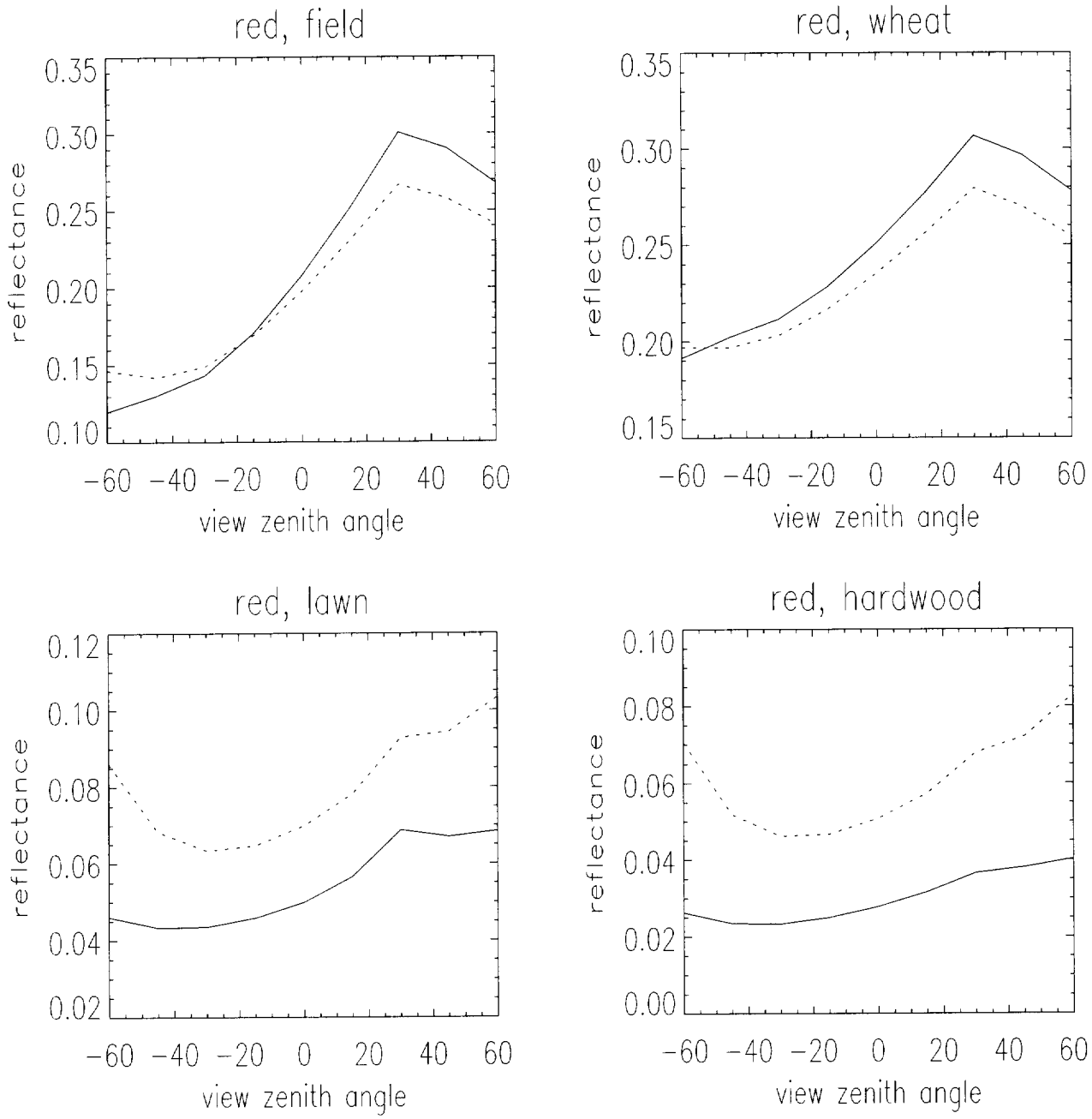

Fig. 5 The BRDF in the Principal Plane for selected Kimes data in the red band, where the sun zenith angle is 30° and aerosol optical depth is 0.2. solid line: true value; dotted line: the value at the top of atmosphere.

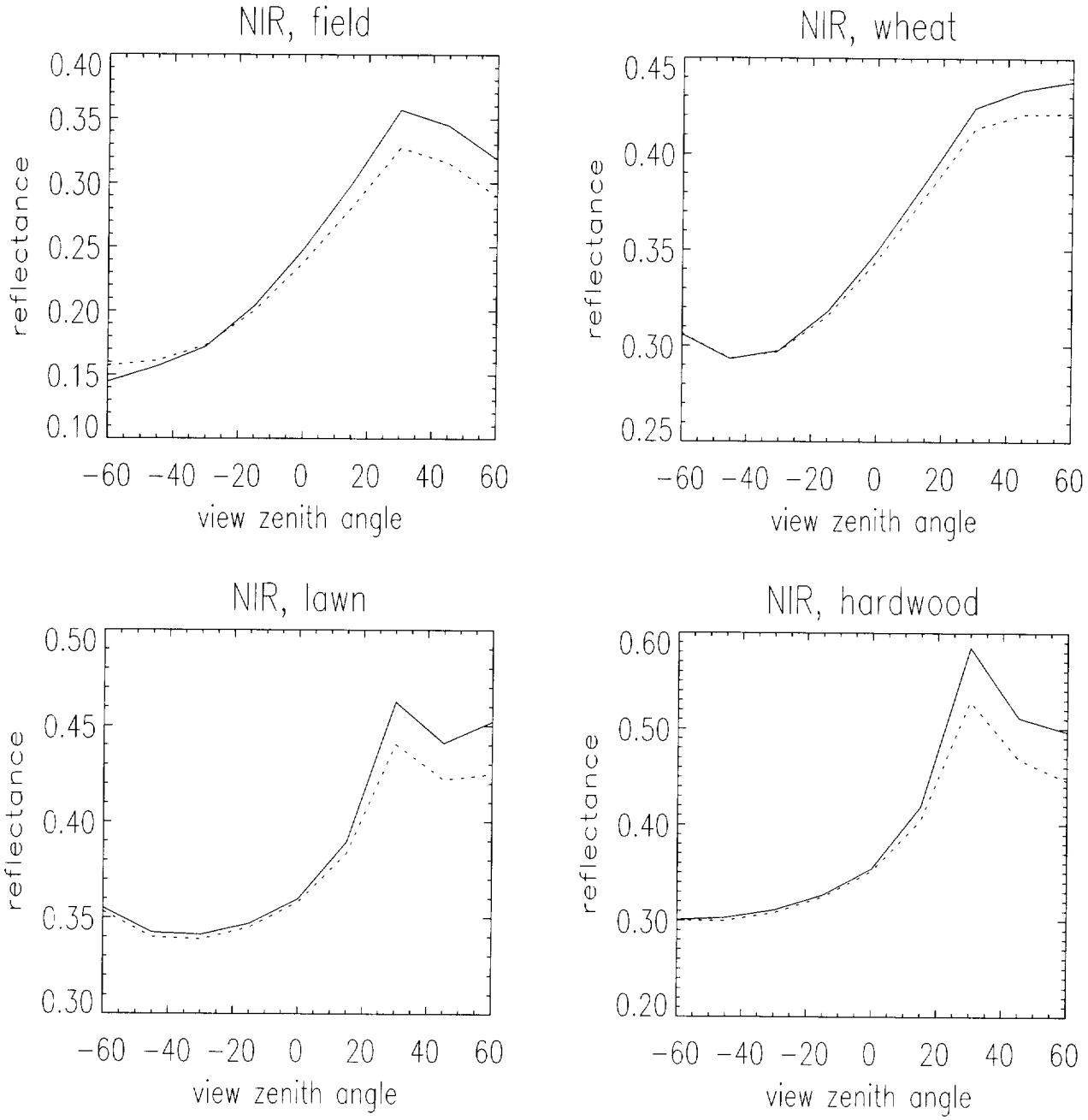

Fig. 6 The BRDF in the Principal Plane for selected Kimes data in the near-infrared band, where the sun zenith angle is 30° and aerosol optical depth is 0.2. solid line: true value; dotted line: the value at the top of atmosphere.

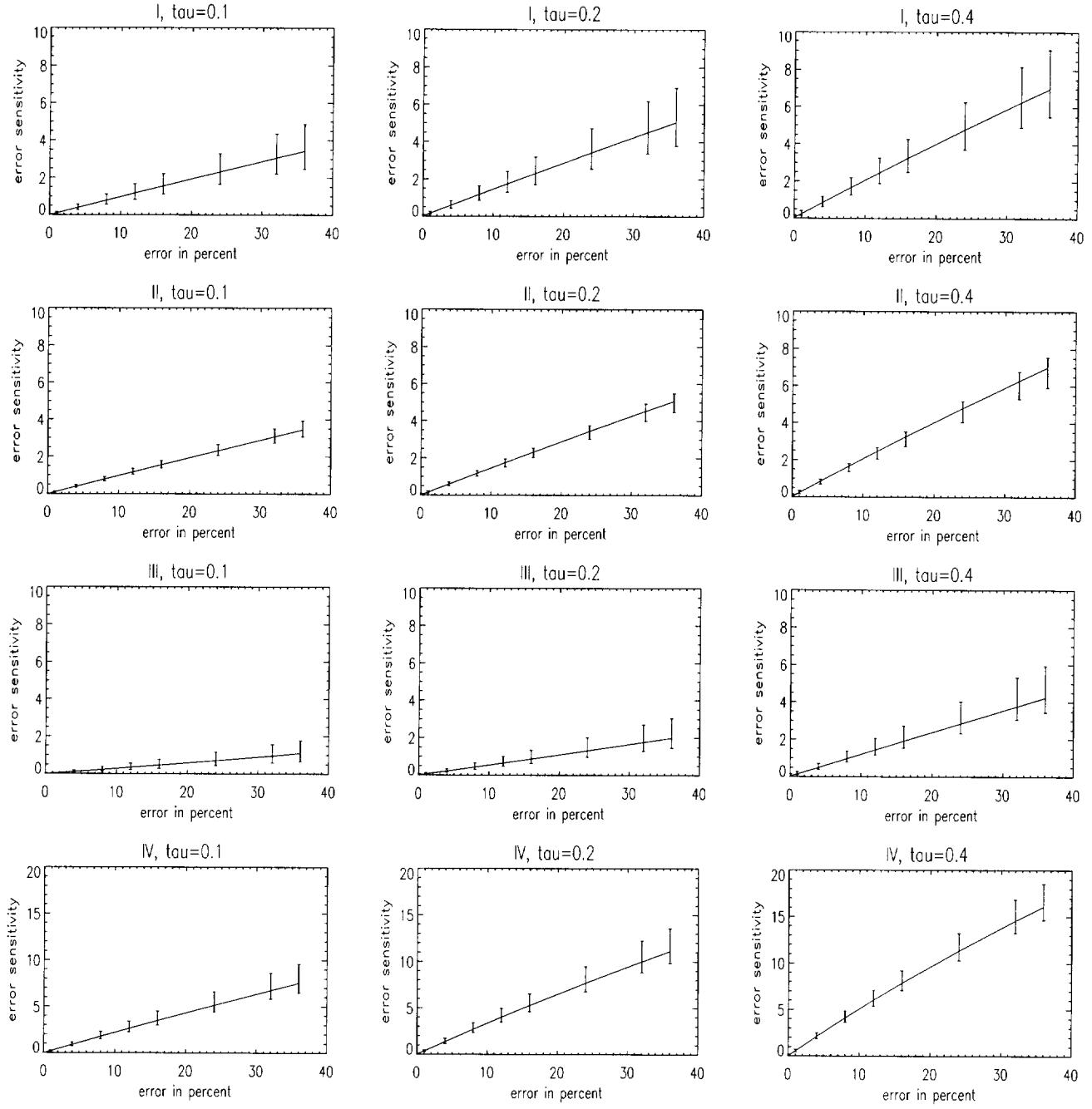

Fig. 7 The sensitivity of the retrieved surface reflectances to $\bar{\rho}^*$(I), $\bar{\rho}'^*$(II), $\bar{\bar{\rho}}^*$ (III) and all of them togather (IV) in the red band

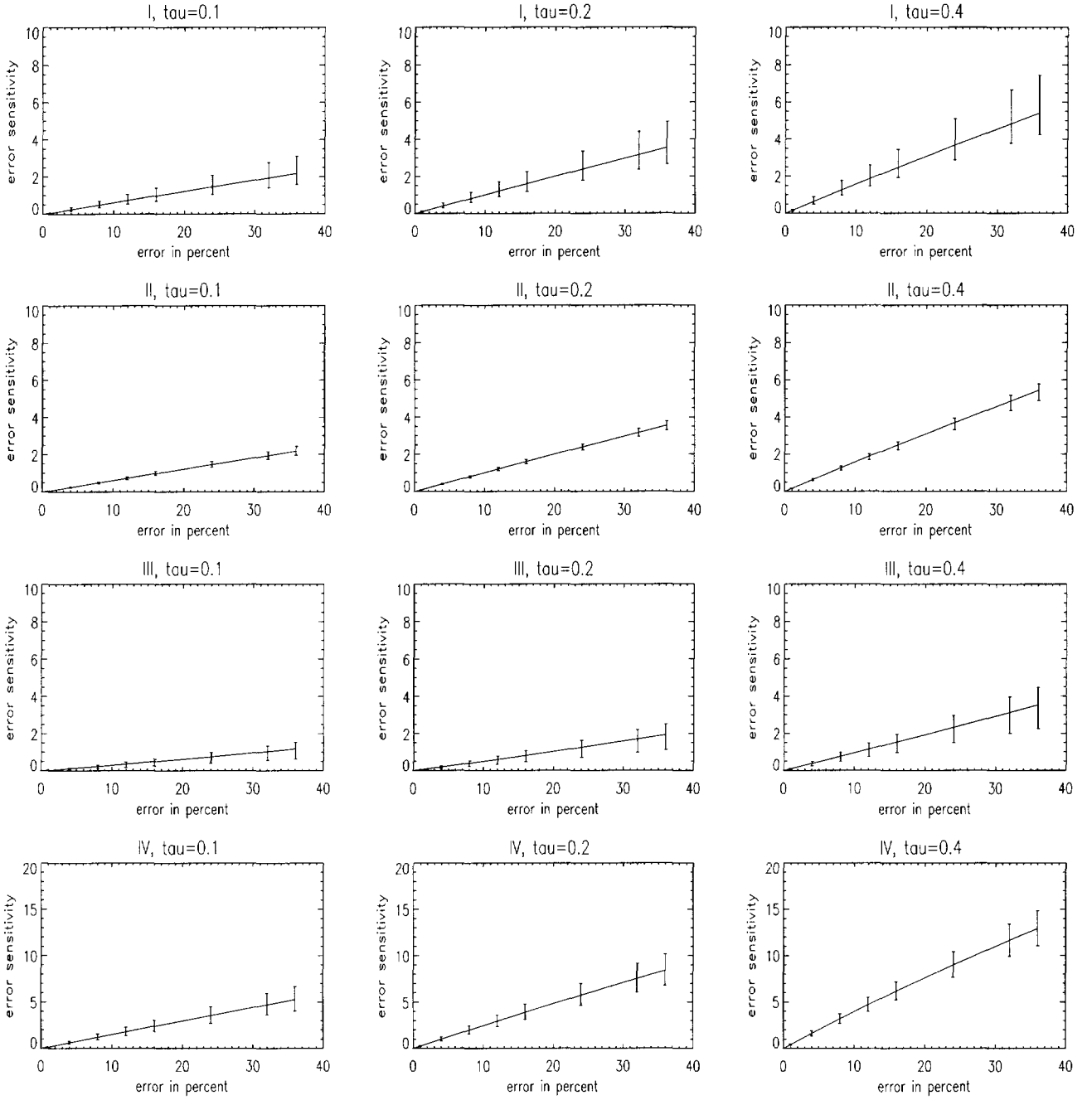

Fig. 8 The sensitivity of the retrieved surface reflectances to $\bar{\rho}^*$(I), $\bar{\rho'}^*$(II), $\bar{\bar{\rho}}^*$ (III), and all of them togather (IV) in the near infrared band

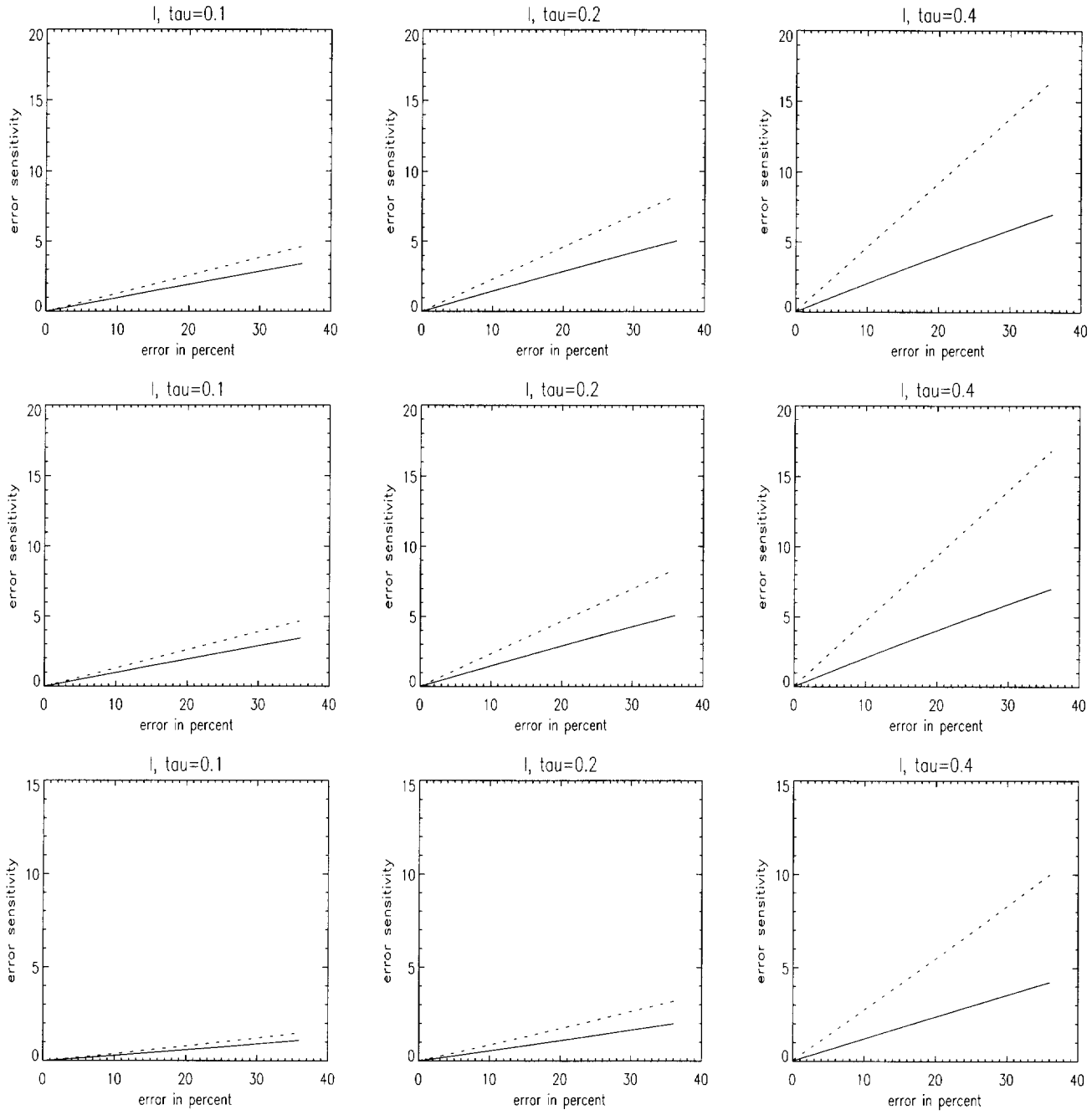

Fig. 9 The comparison between the sensitivity of the retrieved surface reflectances to $\bar{\rho}$(I), $\bar{\rho}'$(II), $\bar{\bar{\rho}}$ (III) (dashed lines) and the sensitivity of the retrieved surface reflectances to $\bar{\rho}^*$(I), $\bar{\rho}'^*$(II), $\bar{\bar{\rho}}^*$ (III) (solid lines) in the red band.